Volume 22
Number 6
11 February 2026
Pages 1283–1474

Soft Matter

rsc.li/soft-matter-journal

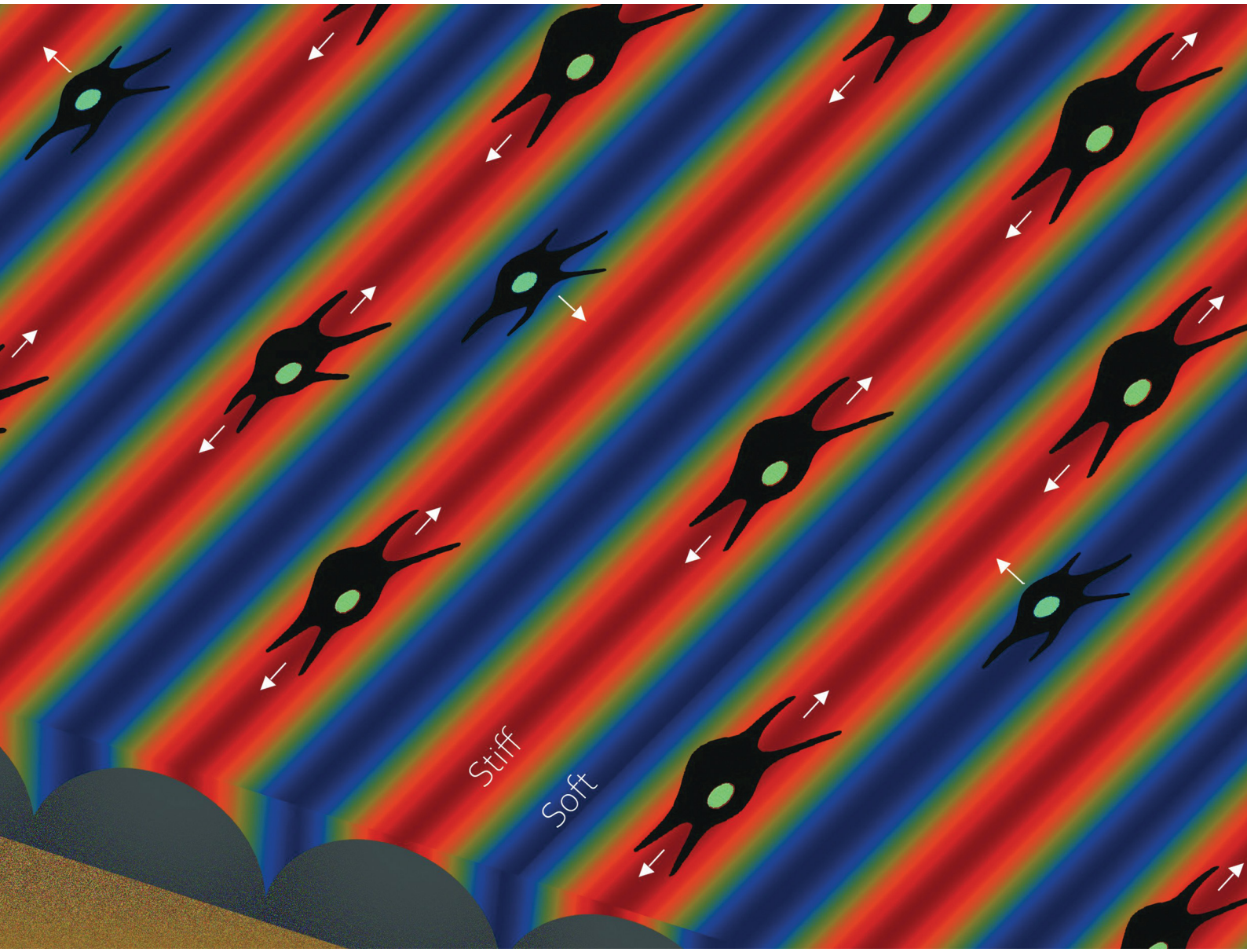

ISSN 1744-6848

ROYAL SOCIETY OF CHEMISTRY

PAPER
Bibhu Ranjan Sarangi *et al.*
Cellular mechanosensing on a cell-scale stiffness gradient substrate

Soft Matter

PAPER

View Article Online
View Journal | View Issue

Check for updates

Cite this: *Soft Matter*, 2026, **22**, 1314

Cellular mechanosensing on a cell-scale stiffness gradient substrate

Indrajit Bhattacharjee,[a] Gautam V. Soni [b] and Bibhu Ranjan Sarangi *[ac]

Received 9th June 2025,
Accepted 29th November 2025

DOI: 10.1039/d5sm00592b

rsc.li/soft-matter-journal

Cells have the ability to sense and respond to various mechanical cues from their immediate surroundings. One of the manifestations of such a process, which is also known as "mechanosensing", is directed cell migration. Various biological processes have been shown to be controlled by extracellular matrix (ECM) stiffness. Substrates with a high stiffness gradient have been used as a platform to investigate cellular motion in response to mechanical cues. However, creating a cell scale stiffness gradient in such a cell adhesion friendly substrate still remains elusive. In this study, we present a simple and versatile method for fabricating substrates with a periodically varying stiffness profile at the cellular scale, featuring customizable high stiffness gradients. Fibroblast cells, when presented with such continuous yet anisotropic variation of stiffness, preferentially position their nuclei in stiffer regions of the substrate and align themselves along the direction of the lowest rigidity gradient. Furthermore, when the rigidity of the substrate is sufficiently high, cells exhibit less sensitivity to stiffness gradients, with their elongation and nuclear positioning becoming independent of stiffness variations. Overall, our experimental results reveal new insights into the process of cellular mechanosensing where the cell-scale gradient drives strong positional and orientational order.

Open Access Article. Published on 17 dicembre 2025. Downloaded on 06/03/2026 20:44:40.
This article is licensed under a Creative Commons Attribution-NonCommercial 3.0 Unported Licence.

1 Introduction

tCells assess the stiffness of their environment by attaching themselves to and exerting force on the surrounding matrix. This mechanosensing influences various cellular processes, including migration, differentiation, proliferation, wound healing, tissue remodeling, and morphogenesis, as well as the progression of disease.[1–9] At the level of individual cells, substrate rigidity affects cell morphology, actin cytoskeleton organization, polarization, and movement. As the substrate becomes stiffer, the actomyosin network within the cell becomes more organized, leading to a shift in cell shape from a nearly circular to a more elongated one. Furthermore, the area of cell adhesion expands with increasing substrate rigidity.[10–12] When exposed to a stiffness gradient, cells are generally known to migrate towards the stiffer regions of the substrate.[13–17] It is also well established that variations in substrate stiffness significantly affect cell orientation and spatial distribution.[18–22]

The investigation of such mechanosensing behaviors often involves a cell adhesion friendly substrate with spatially varying stiffness. Hydrogels are usually used to prepare cell adhesive substrates, as they are easy to functionalize with ECM proteins such as fibronectin. Various methods have been used to produce rigidity gradients in the hydrogel substrate. One of the simple methods is to use the spatial variation of the cross-linker concentration on a length scale through simple diffusion.[23] The variation in cross-linker concentration results in varying degrees of polymerization and, hence, varying stiffness. However, the achievable stiffness gradient value with such a method is typically small (0.001–0.01 kPa μm^{-1}). Diffusion, along with controlled photopolymerization, was also used as a tool to create a stiffness gradient on the hydrogel substrate, and a comparatively higher stiffness gradient (0.01–0.04 kPa μm^{-1}) was reported.[12,24–26] The use of a moving mask with controlled UV exposure during photopolymerization offers an advanced technique for the fabrication of substrates with a stiffness gradient in the range of 0.067 to 0.2 kPa μm^{-1}.[11] By making a junction between two materials in which one is hard and the other is comparable to soft, a step stiffness gradient substrate was developed.[27,28] The majority of the procedures mentioned above provide fairly restricted linear stiffness gradient values or step stiffness gradients, and some of them require quite a complex experimental setup. So far, there has been a lack of studies on substrates with a continuous stiffness gradient at the scale of an individual cell. Producing a high stiffness gradient at the cell scale for studying cellular mechanosensing remains a significant challenge.

[a] *Physical and Chemical Biology Laboratory, Dept of Physics, Indian Institute of Technology Palakkad, Palakkad, 678623, Kerala, India. E-mail: 222014001@smail.iitpkd.ac.in*
[b] *Raman Research Institute, Bangalore, 560080, India. E-mail: gvsoni@rri.res.in*
[c] *Dept of Biological Sciences and Engineering, Indian Institute of Technology Palakkad, Palakkad, 678623, Kerala, India. E-mail: bibhu@iitpkd.ac.in*

This journal is © The Royal Society of Chemistry 2026

Open Access Article. Published on 17 dicembre 2025. Downloaded on 06/03/2026 20:44:40.
This article is licensed under a Creative Commons Attribution-NonCommercial 3.0 Unported Licence.

A relatively recent strategy involves the use of layered substrates in which a soft layer is deposited atop a rigid base. By varying the thickness of the compliant layer over the stiff substrate, stiffness gradients in the range of approximately 0.1–0.25 kPa μm^{-1} have been demonstrated.[29–33] Adhered cells continuously apply forces on their supporting substrate. The way in which the substrate deforms in response is influenced by both its mechanical properties and the amount of force applied. When cells are on a flexible gel that is firmly connected to an infinitely rigid material beneath it, the gel appears to be stiffer. This effect becomes more pronounced as the thickness of the gel approaches the length scale of the deforming region where the deformation occurs.[34–36] When the thickness of the compliant layer is small compared to the lateral extent of cellular traction forces, the rigid base restricts vertical and lateral deformation, leading to an effectively stiffer response.[35]

In this study, we present a novel and accessible method to fabricate cell-adhesion-friendly substrates with exceptionally high stiffness gradients. Our approach is simple, robust, and allows fine tuning of the stiffness gradient at the scale of individual cells. The fabrication relies on using the topography of an underlying glass substrate as a template to generate a controlled stiffness variation within a homogeneous polyacrylamide (PAA) gel layer. This ensures uniform extracellular matrix (ECM) protein attachment while maintaining gradient precision. The method requires only standard laboratory equipment, making it easy to implement. The resulting substrates display steep and tunable stiffness gradients across cellular length scales. Fibroblast cells exposed to an anisotropic stiffness gradient display distinct positional and orientational responses. Our experiments reveal that the nuclei preferentially localize in regions of higher stiffness, while the cells align along the direction of the minimum rigidity gradient. Notably, when the minimum stiffness of the polyacrylamide (PAA) substrate exceeds a threshold value, the cells exhibit diminished responsiveness to the gradient. Overall, we demonstrate a simple yet powerful method for fabricating substrates with tunable, cell-scale stiffness gradients. These substrates offer a versatile platform for probing the physical limits of cellular mechanosensing.

2 Methods

2.1 Substrate fabrication

Our substrate consists of a thin layer of hydrogel deposited on top of an array of glass capillaries of selected diameters assembled on a coverslip. The schematic diagram of the substrate is shown in Fig. 1(a). This substrate preparation process was performed in several steps. The first step involves the preparation of a stiffer bottom substrate, which essentially consists of glass capillaries (Narishige G-1) that were pulled using a micro-pipette puller (Narishige PC-100) to achieve the desired outer diameter. In order to maintain uniformity, we only selected suitable sections of the pulled glass capillaries, verified through the microscope, for further fabrication procedures. The outer diameter of the selected capillaries was 53.9 ± 1.3 μm (see the SI, Fig. S1). In the rest of our discussion, these glass capillaries are referred to as rods, and polyacrylamide gels are referred to as PAA gels. For the assembly of the rods, we first washed the coverslips with 70% ethanol and allowed them to dry at room temperature. After that, the glass rods were aligned on top of the coverslip with the help of very fine tweezers under the microscope. To stabilize the rods on the coverslips, a tiny amount of silicone sealant was used only on the edges as needed.

The coverslips (containing rods) were amino-silanated to facilitate the binding of the PAA gel following standard procedures.[37] Briefly, the glass coverslips (containing rods) were first washed with 70% ethanol and then heated to 80 °C on a hot plate in the presence of a solution of 0.1 M NaOH. Subsequently, 3-aminopropyltriethoxysilane (APTES, Sigma-Aldrich) was added to the solution and allowed to react for 5 minutes. After the reaction, the coverslips were thoroughly rinsed with deionized water to remove any unreacted agents. The coverslips were then immersed in 0.5% (v/v) glutaraldehyde in phosphate-buffered saline (PBS, Sigma-Aldrich) for 30 minutes to facilitate crosslinking. Finally, the coverslips were allowed to air dry at room temperature. We also prepared Chloro-silanated glass slides to be used to flatten the hydrogel layer without attaching to it. Dichlorodimethylsilane (Sigma, USA) was used as a hydrophobic coating on the glass slides.

To create PAA hydrogel films on top of the glass rods, polymer solutions were prepared using acrylamide monomers (Sigma-Aldrich) and bis-acrylamide (Sigma-Aldrich) in deionized water (DI) in specific ratios to obtain the desired stiffness value. In particular, we used 4%, 10%, and 12% (w/v) acrylamide monomers (Sigma-Aldrich) with 0.1%, 0.1%, and 0.25% bis-acrylamide (Sigma-Aldrich) in deionized (DI) water, respectively, to achieve low (~3 kPa), medium (~14 kPa), and high (~56 kPa) ranges of stiffness (see the SI, Fig. S2).[37,38] The mixtures were then degassed under high vacuum for 40 minutes. After degassing, 1 mL of the PAA solution was taken, and 10 μL of 10% (w/v) ammonium persulfate (APS, ICT) along with 1 μL of *N*,*N*,*N*′,*N*′-tetramethylethylenediamine (TEMED, Sigma-Aldrich) was added. The solution was then vortexed to ensure thorough mixing. After that, 10 μL of mixed solution was quickly pipetted onto the top of the coverslip-containing glass rods, and the chlorosilanated glass slide was placed on top of it. In order to ensure the desired thickness of the hydrogel, it was subjected to a compression of 50 g of weight. The solution was polymerized for one hour. The chlorosilanated glass slide was gently detached, and the substrates were rinsed in a Petri dish and kept in deionized (DI) water for future use. Substrates containing rods with PAA solutions of 4% acrylamide monomers and 0.1% bis-acrylamide, 10% acrylamide monomers and 0.1% bis-acrylamide, and 12% acrylamide monomers and 0.25% bis-acrylamide are hereafter referred to as S-1, S-2, and S-3, respectively.

To verify the thickness of the PAA gel on top of the glass rods, 0.25 μm Tetraspek fluorescent beads (Thermofisher, USA) were embedded in the gel, and cross-sectional images of the

Open Access Article. Published on 17 dicembre 2025. Downloaded on 06/03/2026 20:44:40.
This article is licensed under a Creative Commons Attribution-NonCommercial 3.0 Unported Licence.

substrate (S-1) were taken with a confocal microscope (Olympus flv-3000) using a 10× objective. The minimum gel thickness was found to be on the order of ∼6 μm (Fig. 1c and d). A theoretical estimation of the thickness variation was performed based on the geometry of the arrangements, using the following equation.

$$h = h_0 + \left(r - \sqrt{r^2 - y^2}\right) \quad (1)$$

where h is the thickness of the PAA gel at a distance y from the peak of the rods. h_0 is the minimum thickness of the PAA film just above the peak of the rods, taken as the origin, and r is defined as the radius of the rods. Fig. 1d shows both theoretical and experimental data of the film thickness corresponding to a rod radius of 28 μm. h_0 was measured to be around 6 μm. The surface topography of the substrates was also verified using atomic force microscopy (AFM) scans (see the SI, Fig. S1). The surfaces were found to be smooth, with no significant height variations detected within the scanned area (scan size: 120 μm × 120 μm).

2.2. Characterization of the stiffness gradient

The stiffness of the substrates is characterized by measuring the Young's modulus (E), for which atomic force microscopy (AFM)(Oxford Instruments) was used with a colloidal AFM probe (Novascan). The AFM probe consisted of a polystyrene bead with a diameter of 4.5 μm, attached to silicon nitride cantilevers with a nominal spring constant of ∼44 pN nm^{-1} that were used to measure the stiffness variation on S-1 substrates, while stiffer cantilevers with a spring constant of ∼400 pN nm^{-1} were chosen for the S-2 and S-3 substrates to accommodate their higher stiffness variation. The bulk stiffness of the PAA gels of substrates S-1, S-2, and S-3 was measured using the same AFM probes to ensure consistency across the experiments. The spring constant of the cantilever was determined through calibration using the thermal fluctuation method.[39] Force–distance (F–d) curves were acquired in a liquid medium on substrates for each combination (n = 3 per condition), covering a scan area of 108 μm × 108 μm across a 28 × 28 grid. Furthermore, additional measurements were conducted to measure the bulk stiffness of the PAA gels

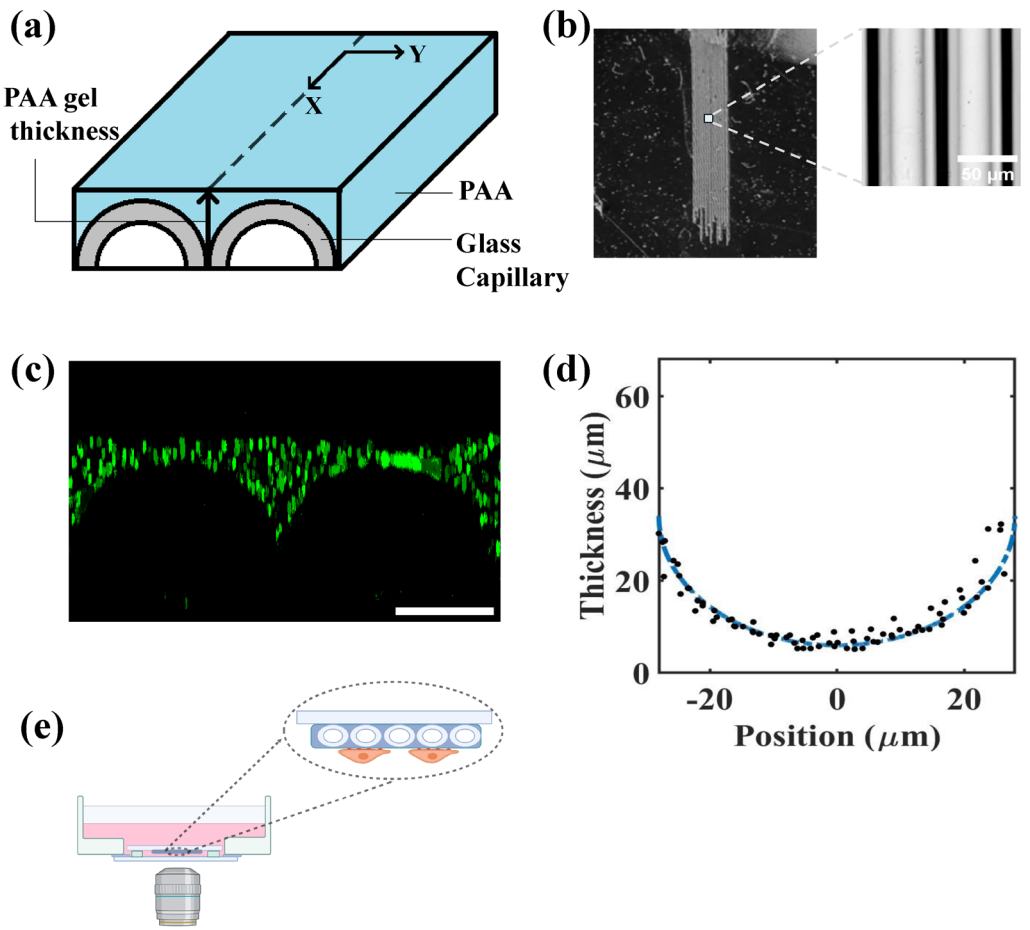

Fig. 1 Substrate fabrication and imaging: (a) a schematic diagram of the substrate, where gray colored half circles are rods (glass capillaries) and the blue is the PAA gel on top of it. (b) The image of the substrate and microscopy image of the rods. (c) Confocal microscopy images showing the cross sectional view of the substrate (S-1) with rods. (d) The measured thickness (dots) and theoretical thickness from the geometry (dashed line) of the PAA film. The thickness of the PAA film varies smoothly in accordance with the underlying surface topography. (e) Illustration of the cross-sectional layout for imaging cells in an upside-down position. The substrate is shown in between two coverslips. Scale bar = 25 μm.

 This journal is © The Royal Society of Chemistry 2026

Open Access Article. Published on 17 dicembre 2025. Downloaded on 06/03/2026 20:44:40.
This article is licensed under a Creative Commons Attribution-NonCommercial 3.0 Unported Licence.

corresponding to each substrate's composition (n = 3 per condition), with the same scan area of 108 μm × 108 μm across a 10 × 10 grid (see the SI, Fig. S2).

The AFM data analysis was performed using a custom-built Matlab program.[40,41] In short, the approach and retract curves were extracted from each raw AFM data set, and the indentation depth (h) was calculated for different applied forces, defined as $h = d - D$, where d is the sample displacement and D is the deflection of the cantilever. Force (P) *vs.* indentation depth (h) plots were analyzed using the Oliver–Pharr method for the spherical probe. Briefly, the peak force of the indenter, the peak displacement, and the slope of the unloading curve were used to compute the reduced modulus (E_r) using the following equation:

$$E_r = S\frac{1}{2\beta}\sqrt{\frac{\pi}{A}} \quad (2)$$

where S is the contact stiffness calculated from the slope dP/dh of the upper portion of the retract curve, β is a factor that accounts for large strain and non-axisymmetry of the indenter and is taken as unity, and A is the contact area defined as:

$$A = \pi(2Rh_c - {h_c}^2) \quad (3)$$

Here, R is the radius of the tip and $h_c = (h_m - h_s)$, where h_m is the maximum indentation depth and $h_s = \varepsilon\frac{P_m}{S}$, with $\varepsilon = 0.75$ for a spherical indenter, and P_m is the maximum load. Young's modulus E was calculated from the reduced modulus E_r using the equation:

$$E = E_r(1 - \sigma^2) \quad (4)$$

where σ is the Poisson's ratio of the PAA gel, taken as 0.3 for the S-1 and S-2 substrates, and 0.5 for the S-3 substrates.[42] All plots were created using Matlab.

2.3 Substrate functionalization

To facilitate cell adhesion, Sulfo-SANPAH-mediated succinimide crosslinking was used to covalently attach fibronectin to the PAA hydrogels.[43] In brief, a solution of 0.2 mg mL^{-1} Sulfo-SANPAH in HEPES buffer (pH 8.5) was added to the substrate, which was then exposed to UV light for 30 minutes to facilitate the reaction. The substrate was then rinsed with 50 mM HEPES buffer, and the process was repeated to ensure efficient protein binding. Subsequently, 50 μL of Bovine Plasma Fibronectin (0.2 mg mL^{-1}) (Thermo Fisher Scientific) was added to the substrate and incubated for 5 hours to allow sufficient time for fibronectin binding.[44] Finally, the substrate was thoroughly rinsed with HEPES to remove excess fibronectin and stored in PBS at 4 °C for further use.

2.4 Cell culture and imaging

Fibroblasts (3T3) were maintained in DMEM 10% fetal bovine serum (HIMEDIA) and supplemented with 80 U penicillin, 80 μg streptomycin, and 0.2 μg of Amphotericin B per mL in 37 °C with 5% CO_2. For immunostaining, cells were seeded in 35 mm Petri dishes containing the prepared fibronectin-coated substrates. The seeding density was approximately 35 cells per mm^2. After 24 h of incubation, the cells were fixed with 4% paraformaldehyde for 30 min at room temperature and washed with 1× PBS (containing 0.05% Tween-20) three times, each for 5 min. The cells were then permeabilized with 0.3% Triton X-100 for 15 min at room temperature and washed with 1× PBS (containing 0.05% Tween-20) three times. For cell nucleus staining, DAPI (Sigma-Aldrich) was used at a concentration of 1 μg mL^{-1} in 1× PBS for 5 min and then washed three times. For actin staining, we used the ActinRed™ 555 ReadyProbes™ Reagent (Rhodamine phalloidin from Thermo Fisher Scientific) for a 1 hour incubation and washed it three times. In order to avoid aberrations while imaging directly through the rods and to make the high NA objectives usable, custom imaging setups were used for both fixed-cell and live-cell imaging. For fixed cells, the substrates along with the fixed cells were inverted over a mounting solution (Sigma-Aldrich) containing cover glasses with spacers (No 1 coverslip was used as a spacer, providing a thickness ∼ 170 μm). Images were acquired using a confocal microscope with 10× and 20× objectives and suitable combinations of lasers and fluorescence filters. Images from various positions of the substrate were stitched together for further analysis of the entire substrate area.

For live cell imaging, CO_2 independent media (Thermo Fisher Scientific) have been used. Cells were first seeded with a similar density of approximately 35 mm^{-2} on the substrate inside a 35 mm petridish. In order to facilitate adhesion to the substrate, the cells were incubated on the substrate for two hours. We used the SiR-Actin Kit (Cytoskeleton, Inc.) and Hoechst (Thermo Fisher Scientific) for actin and nuclei staining, respectively. Live cell images were acquired using a 20× air objective of a confocal system equipped with a live cell imaging setup (Tokai Hit). CO_2 independent medium (Thermo Fisher Scientific) was used in the live cell chamber. For live cell imaging of cells on the substrates, the observation area of the glass bottom petridish (ibidi, μ-Dish 35 mm) was modified with spacers made from thin glass pieces (∼ 170 μm) derived from broken No. 1 coverslips. Then, the substrate containing the cells was inverted onto it (Fig. 1e). This setup allowed for the use of high numerical aperture (NA) objectives with the substrates, enabling high-quality live-cell imaging of the actin cytoskeleton. The images were captured at 5-minute intervals for approximately 36 hours.

2.5 Image analysis

The fluorescence images of fixed-cell nuclei and F-actin on various substrates, as well as the frame corresponding to 24 hours post-seeding extracted from the live-cell recordings, were analyzed using open-source ImageJ software (National Institutes of Health, USA). The merged images of the cells on the substrates were aligned horizontally through a rotational transformation to enable the measurement of the orientation angle. The regions (mostly at the edges) where the alignment of the rods was non-uniform were excluded from our analysis to avoid substrate non-uniformity effects. The cropped images of fluorescently labeled nuclei were thresholded and masked

Open Access Article. Published on 17 dicembre 2025. Downloaded on 06/03/2026 20:44:40. This article is licensed under a Creative Commons Attribution-NonCommercial 3.0 Unported Licence.

using the analyze particles tool for a particular particle size. The image segmentation was performed using the Star Disk segmentation tool plugin in ImageJ.[45] Subsequently, using particle analysis tools, all the nuclear positions were extracted. In addition, from the bright field images, the peak position of the rods was extracted. To find the distribution of nuclei on the substrates, we analyzed this data using a custom-built Matlab program. Each nucleus was mapped uniquely to the nearest rod, thus avoiding overcounting. With a bin size of 7 μm, the number of nuclei belonging to each bin was counted and normalized with the total count. The orientational distribution of the cells on the substrates was analyzed by thresholding the cropped fluorescently labeled f-actin images of the cells. Individual cells were manually selected and fitted with an ellipse, and the angle(θ) between the major axis and the horizontal axis was measured.

To obtain the orientational information of both cells and nuclei, all positions of all the cells and their corresponding nuclei are extracted. The center of mass (COM) was determined by fitting an ellipse to the thresholded images of both cells and nuclei. Along with that, their orientational angle was determined by measuring the angle between the ellipse major axis and the rod's long direction. The distance between the center of mass (COM) of the cells and the corresponding nuclei was determined using the following equation:

$$\text{Distance} = \sqrt{(x_{\text{COM,cell}} - x_{\text{COM,nuclei}})^2 + (y_{\text{COM,cell}} - y_{\text{COM,nuclei}})^2} \quad (5)$$

The distribution of the difference between the orientation angles of the cells and the corresponding orientation angles of their nuclei was plotted. The cell aspect ratio was calculated as the ratio of the major axis to the minor axis of the ellipses fitted to the cells. Additionally, the circularity and aspect ratio of the cell nuclei, as well as the cell spreading area, were quantified with respect to each cell's relative position from the peak of the rods. The comparisons of the cell spreading area were also performed on the soft ($\sim$3 kPa), stiff ($\sim$56 kPa) and gradient substrates (S-1).

Time lapse fluorescence microscopy images of live cells were analyzed using ImageJ software to track individual cells. Initially, the sequential images of the nuclei of the cells were thresholded and masked using the analyze particles tool to remove all other backgrounds. Then the trajectories of individual cell nuclei were tracked through TracKMate software Plugin in ImageJ.[46] After the positional data of the nuclei were obtained along with the frames, the peak positions of the rods were taken from the bright-field images. Using a custom-built Matlab program, the speed of the cells in different positions and the location-based dwell time were calculated, considering the distance from the nearest rods. After that, corresponding to these shortest distances, the horizontal component (along the rods) and vertical component (perpendicular to the rods) of the speed of the nuclei were calculated. Then these distances were binned to the 4 μm interval from the peak of the rods, along with the corresponding speed components. To calculate the average migration speed along the horizontal and vertical directions in different locations, the mean of the speed components was taken within each 4 μm bin size. The dwell time based on the location of the cell nuclei was analyzed within individual bins from the time lapse images. The distribution of the speed components within each 7 μm region was also obtained (see the SI, Fig. S5). In total, more than 80 cell tracks were observed across four replicates of S-1 substrates, over an approximate period ranging from 8 h to 37.5 h. All plots were prepared using Matlab.

2.6 Statistical analysis

The AFM data are reported as the mean ± standard deviation (SD), while all other data are expressed as mean ± standard error (SE). All experiments were performed in triplicate unless stated otherwise, and the number of cells included in each measurement is indicated where applicable. The statistical significance was assessed by One-Way ANOVA followed by Tukey's HSD *Post hoc* Test (pairwise comparisons); for all: $*P < 0.05$, $**P < 0.002$, $***P < 0.0002$, $****p < 0.000001$; ns $p > 0.05$, not significant.

3 Results and discussion

3.1 Topography mediated stiffness variation

Cells have the ability to sense the rigidity of the underlying substrate up to a few microns.[34] So, it is crucial to ensure that the thickness of the PAA gel film does not exceed a few micrometers. As described in the previous section, our confocal imaging of the substrate embedded with fluorescent beads allowed us to characterize the thickness of the hydrogel film on top of the rods. The film thickness was found to be $\sim$6 μm at the peak position of the rods, which is optimal for cells to sense the effects of the underlying hard substrate. The periodicity and continuous variation in the thickness of the PAA films are clearly evident from the height profile observed in the fluorescent images. Furthermore, the thickness variation observed in the fluorescent cross-sectional image closely matched the theoretical height calculations based on the geometry of the film, indicating a smooth and consistent change in height (Fig. 1c and d). The height profile of the PAA films from the fluorescent images showed a maximum thickness of around 32 μm in the middle between the two rods and gradually decreased toward the peak of the rods. AFM topography images of the substrates revealed an approximate height variation of 4 μm over a scan area of 120 μm × 120 μm. It has been previously reported that, in the absence of pronounced valleys or hills, surface topography does not significantly influence the cell migration process, even when the height difference is on the order of several tens of microns.[47,48] Therefore, the surface of the substrates was considered homogeneous, with no significant height differences that could affect cell migration. Consequently, any observed differences in cell migration behavior can be attributed predominantly to variations in substrate stiffness rather than to surface topography (see the SI, Fig. S1).

 This journal is © The Royal Society of Chemistry 2026

Open Access Article. Published on 17 dicembre 2025. Downloaded on 06/03/2026 20:44:40.
This article is licensed under a Creative Commons Attribution-NonCommercial 3.0 Unported Licence.

To characterize the mechanical properties of the prepared substrates, atomic force microscopy (AFM) was used. Three distinct types of stiffness in PAA gels were polymerized on top of the rods to produce substrates having a tunable range of stiffness gradients. The bulk stiffness of the PAA gels, modulated by varying the acrylamide and bis-acrylamide concentrations, was measured to be around ~3 kPa (S-1 substrate), ~14 kPa (S-2 substrate), and ~56 kPa (S-3 substrate), thereby categorizing the substrates into discrete stiffness regimes: low (S-1), intermediate (S-2), and relatively high (S-3) stiffness conditions. This approach provides controlled, mechanically heterogeneous microenvironments at the single-cell scale. The stiffness map covers a scan area of 108 μm × 108 μm across a 10 × 10 grid of the uniform substrates (see the SI, Fig. S2). Stiffness mapping of the stiffness gradient substrates S-1, S-2, and S-3 indicates that the variation in substrate stiffness correlates with the film thickness of the PAA gel, transitioning from stiffer to softer from the peak of the rods to the midpoint between the two adjacent rods (Fig. 2a–c). The stiffness values at the peak of the rods were found to be 35 ± 2 kPa, 54 ± 8 kPa, and 447 ± 38 kPa for the S-1, S-2, and S-3 substrates, respectively. Moving laterally away from the peaks, the stiffness values gradually decreased on both sides of the peak, reaching a minimum of around 3.0 ± 0.1, 14.0 ± 0.4, and 56 ± 4 kPa at the midpoint between the two rods for the S-1, S-2, and S-3 substrates, respectively (Fig. 2d–f). This minimum value was

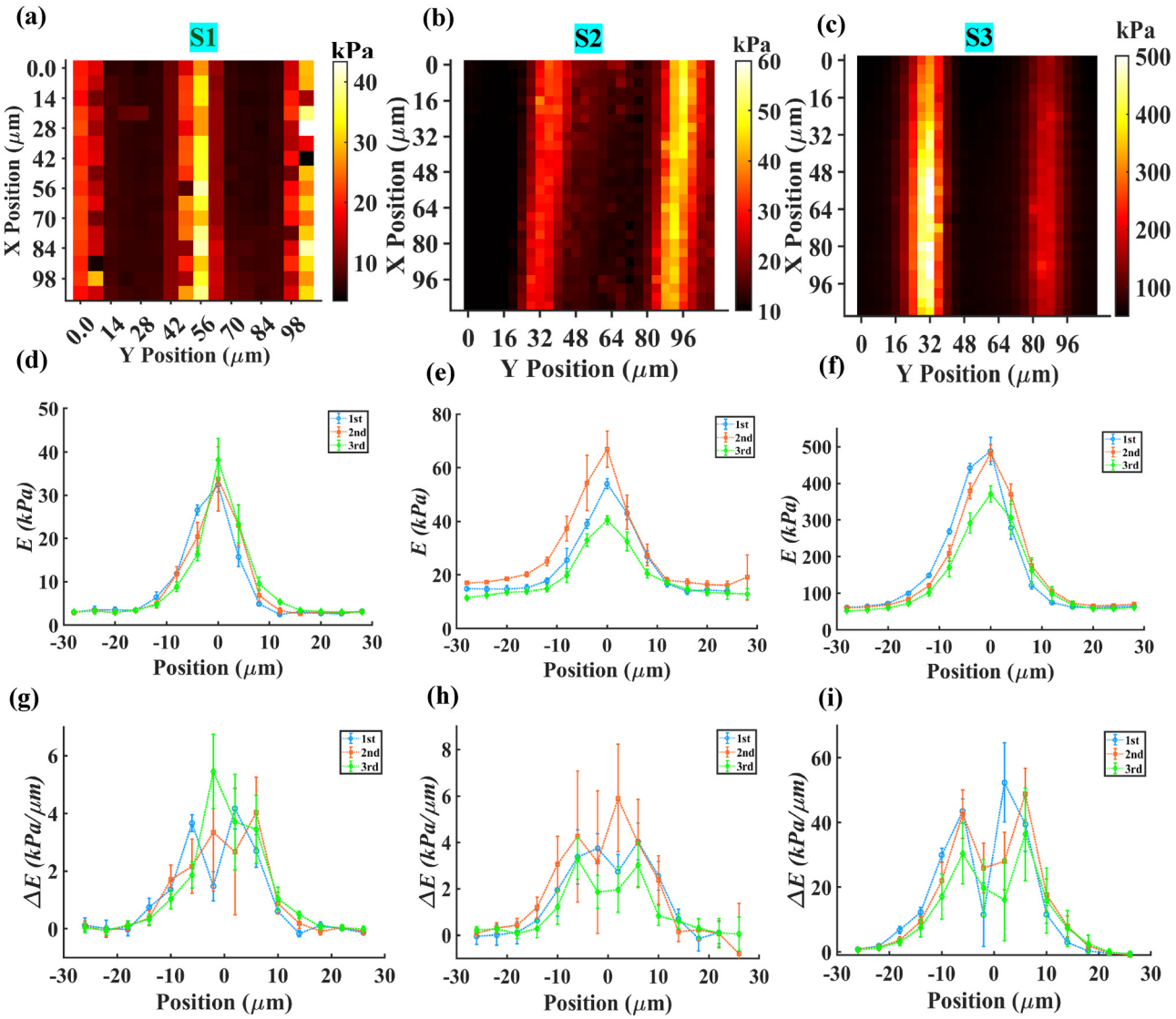

Fig. 2 Characterization of the mechanical properties of the substrate: (a) stiffness map (105 μm × 105 μm) of the S-1 substrate and (b) and (c) the stiffness map of the substrates S-2 and S-3, respectively (scan area 108 μm× 108 μm, across a 28 × 28 grid). (d)–(f) Depict the variation of rigidity across the rods of the substrates S-1, S-2, and S-3, respectively (n = 3 replicates for each substrate). Variation of the stiffness is consistent with the variation of the PAA film thickness and it crucially depends on the composition of the PAA gels used for fabrication of the substrates. Furthermore, the lowest apparent stiffness is comparable with the bulk rigidity of the PAA gels of the substrates. (g)–(i) Spatial Variation of the stiffness gradient across the rods of the substrates S-1, S-2, and S-3, respectively (n = 3 replicates for each substrate). The error bars represent the standard deviation of the data.

Open Access Article. Published on 17 dicembre 2025. Downloaded on 06/03/2026 20:44:40.
This article is licensed under a Creative Commons Attribution-NonCommercial 3.0 Unported Licence.

comparable to the bulk stiffness of the PAA gel of the substrate (see the SI, Fig. S2).[37] The maximum stiffness gradient, observed across the region surrounding the peak of the rods, was $\sim$46 kPa μm^{-1} for the S-3 substrate. In comparison, the corresponding values for the S-1 and S-2 substrates were found to be $\sim$4.5 kPa μm^{-1} and $\sim$4.4 kPa μm^{-1}, respectively. Notably, this gradient value gradually decreased toward the midpoint between the two rods (Fig. 2g–i). Therefore, from the above observations, it can be concluded that the stiffness of the substrate varies periodically in correlation with the film thickness across the rods. As the thickness of the PAA film decreases, the stiffness increases, and *vice versa*. Furthermore, by varying the composition of PAA gels with the rods, a wide and tunable range of stiffness gradient substrates was produced. One of the important aspects of our observation is that the substrate stiffness at any position is crucially dependent on the film thickness at that position. Overall, our experimental observation suggests that the film thickness and, hence, the topography of the substrates' underlying rods dictate, the local stiffness value and the associated gradient at that position.

3.2 Positional and orientational distribution

In order to investigate the effect of spatial inhomogeneity of stiffness on cellular position and orientation, we used 3T3 fibroblast cells on substrates with a tunable cell scale stiffness gradient, as mentioned in the methodology. We used the fluorescence microscopy data to quantify the positions and orientations of the cells. Fluorescent images of cell nuclei, captured 24 hours after seeding on the substrate, showed that most of the cell nuclei were concentrated in the region of hydrogel near the peaks of the rods. This region, as mentioned previously, corresponds to the highest stiffness due to the smallest thickness of the PAA film (Fig. 3a and d). From the distribution of cell nuclei in different positions on the substrates S-1 and S-2, it was found that 46 $\pm$ 4% and 55 $\pm$ 15% of the nuclei were located within $\pm$ 7 μm around the peak of the rods, respectively. This distribution rapidly decreased towards the middle region between the two rods. Only 12 $\pm$ 6% and 11 $\pm$ 6% of the cell nuclei were found in areas farther from the peak, specifically between $\pm$ 21 μm to $\pm$ 28 μm on the substrates S-1 and S-2, respectively (Fig. 3b and e).

Moreover, we investigated the influence of the asymmetric stiffness gradient produced by the substrate on the orientation of the cells. The angular plots present the cell orientational distribution from 0° to ±90°, hence only considering the acute angles. 0° represents the direction along the rods and ±90° represents the angle perpendicular to the orientation of the rods. Approximately 75% and 68% of the cells were found to have an orientation angle of ±30° when they were seeded on substrates S-1 and S-2, respectively, which coincides with the direction of the low rigidity gradient (Fig. 3c and f). In addition, they also elongated themselves in the direction of the minimum rigidity gradient, which is along the rods (Fig. 3a and d).

In order to understand the effect of both local stiffness and the associated stiffness gradient, we prepared a substrate S-3 using rods of the same diameter and, hence, the same topographical features, but with a PAA film that has a high bulk stiffness ($\sim$56 kPa). On this substrate, we observed contrasting behavior regarding both the position and orientation of the cells. The cell nuclei were distributed uniformly throughout the substrate, indicating no preference for specific regions (Fig. 3h). It was evident that cells attempted to position their nuclei on the stiffer parts of the substrate. However, when the stiffness of the PAA gel was sufficiently high, cells no longer showed a preference for positioning their nuclei based on the substrate's effective stiffness. We also observed a nearly uniform orientational distribution on this substrate (Fig. 3i).

From the comparative study mentioned above, it is evident that beyond a certain value of local stiffness, the gradient effects become less prominent. We expect this value of stiffness to depend on the cell type. Fibroblast cells have a typical value of 5 kPa to 17 kPa depending on the part of the cell.[49] It has also been predicted that cells adapt to the ECM stiffness by modulating their own stiffness. We believe that beyond a certain threshold stiffness, this mechanism may reach saturation, thereby making the cell insensitive to variations in stiffness.

Furthermore, we analyzed the relative positions and orientations of cell nuclei with reference to the center of mass of the cell (Fig. 4a and b). Most of the cells on this patterned substrate S-1 showed elongated morphology (Fig. 4c). Interestingly, the nucleus position showed a measurable shift from that of the center of mass of the cell (Fig. 4e). This may indicate the existence of a phase lag between the movements of the nucleus and the cell. Previous studies indicate that the nuclei preferentially position themselves at the rear end of the cell during migration.[50] Interestingly, we find a strong correlation between the orientations of the nucleus and the cell (Fig. 4d). The shape of the nucleus is adaptive and may result from the ordering of the cytoskeletal network of the cell. The anisotropy of this patterned substrate (S-1) drives the polarity observed in the mechanosensing network inside the cell, which, in turn, drives both cell and nuclear polarity, as observed in our experiments. From the measurements of nuclear circularity, nuclear aspect ratio, and cell spreading as a function of each cell's relative position from the peak of the rods (S-1), these parameters appear uniform. This supports the view that the stiffness-gradient length scale is comparable to the cell dimension, such that each cell simultaneously experiences a continuum of stiffness values across its body. Moreover, comparisons of cell spreading on the soft ($\sim$3 kPa), stiff ($\sim$56 kPa), and gradient (S1) substrates show that the spreading area on the gradient substrate falls between the two extremes, consistent with this interpretation (see the SI, Fig. S3). It is well established that actin organization is sensitive to substrate rigidity, as demonstrated in studies showing rigidity dependent cytoskeletal alignment.[2,10] However, on a substrate with an asymmetric rigidity gradient, no global ordering is favoured. Instead, the actin network exhibits locally ordered domains rather than a uniform orientation (see the SI, Fig. S4).

 This journal is © The Royal Society of Chemistry 2026

Open Access Article. Published on 17 dicembre 2025. Downloaded on 06/03/2026 20:44:40.
This article is licensed under a Creative Commons Attribution-NonCommercial 3.0 Unported Licence.

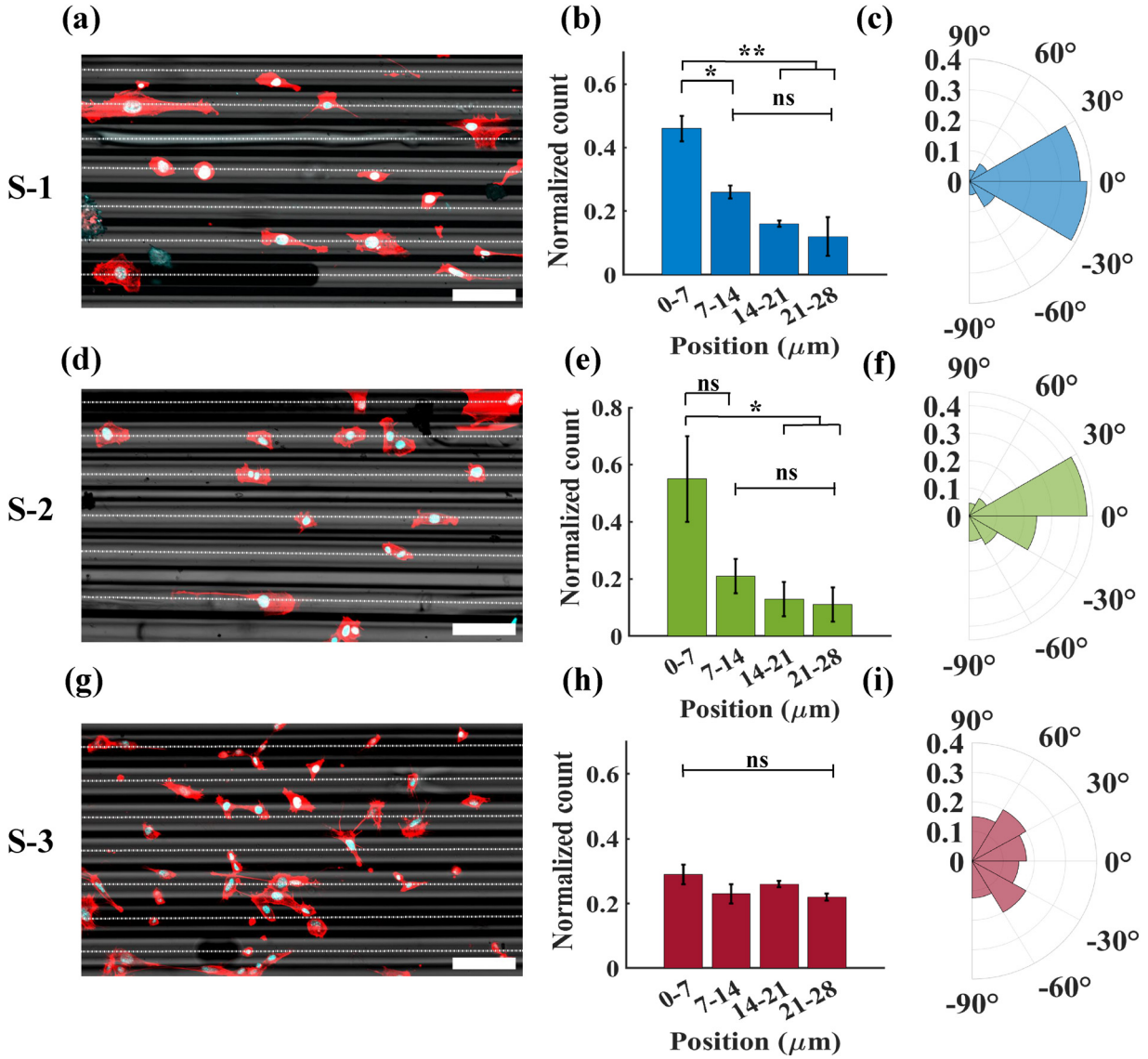

Fig. 3 Positional and orientational distribution: (a), (d) and (g) Superimposed fluorescence images of 3T3 fibroblast cells on the fibronectin-coated rigidity-gradient substrates S-1, S-2, and S-3, respectively. Rods are in gray, cell nuclear DNA was stained with DAPI (cyan) and f-actin was stained with phalloidin (red). Dashed lines indicate the peaks of the rods, which correspond to the highest stiffness region. (b), (e) and (h) The distribution of cell nuclei across the rods of the substrates S-1 ($N > 200$ cells over $n = 3$ replicates), S-2 ($N > 300$ cells over $n = 3$ replicates), and S-3 ($N > 300$ cells over three regions of $n = 2$ replicates), respectively, with a bin size $\pm$ 7 μm from the peak of the rods taken as a reference point. (c), (f) and (i) Angular distribution of the cells' orientation on the substrates S-1, S-2 ($N > 110$ cells over $n = 3$ replicates of S-1 and S-2) and S-3 ($N > 50$ cells over $n = 2$ replicates), respectively. When cells were seeded on S-1 and S-2 substrates, most of the cell nuclei were positioned near the peaks of the rods and oriented along the rods (minimum stiffness gradient direction). In contrast, the nuclei distribution and cells' orientational distribution were uniform, regardless of the substrate's stiffness variation when cells were seeded on the S-3 substrates. The statistical significance was assessed by one-way ANOVA followed by Tukey's HSD *Post hoc* test (pairwise comparisons) and for all: *$P < 0.05$, **$P < 0.002$; ns $p > 0.05$., not significant. Error bars are represented here as SE. Bin size is 30°. Scale bar = 100 μm.

3.3 Role of local stiffness and stiffness gradient in cell migration and location-specific dwell time

Time-lapse images of the fluorescence-labeled cell nuclei and the substrate were recorded for 3T3 fibroblast cells grown on the substrate (S-1) over a period of approximately 36 hours. Using tracking algorithms, as mentioned in the methodology, the position of the cell nuclei was extracted as a function of time (supplementary movie). From the trajectory of the nuclei, it is apparent that the spatial inhomogeneity, both in stiffness and stiffness gradient, influences the migration in a significant way. To quantify this, we analyzed the vertical (perpendicular to the rod) and horizontal (along the rod) migration speeds at different locations, taking the peak of the rods as our reference point for distance.

As evident from our experiments, both the horizontal speed (V_x) and the vertical speed (V_y) are influenced not only by the

Open Access Article. Published on 17 dicembre 2025. Downloaded on 06/03/2026 20:44:40.
This article is licensed under a Creative Commons Attribution-NonCommercial 3.0 Unported Licence.

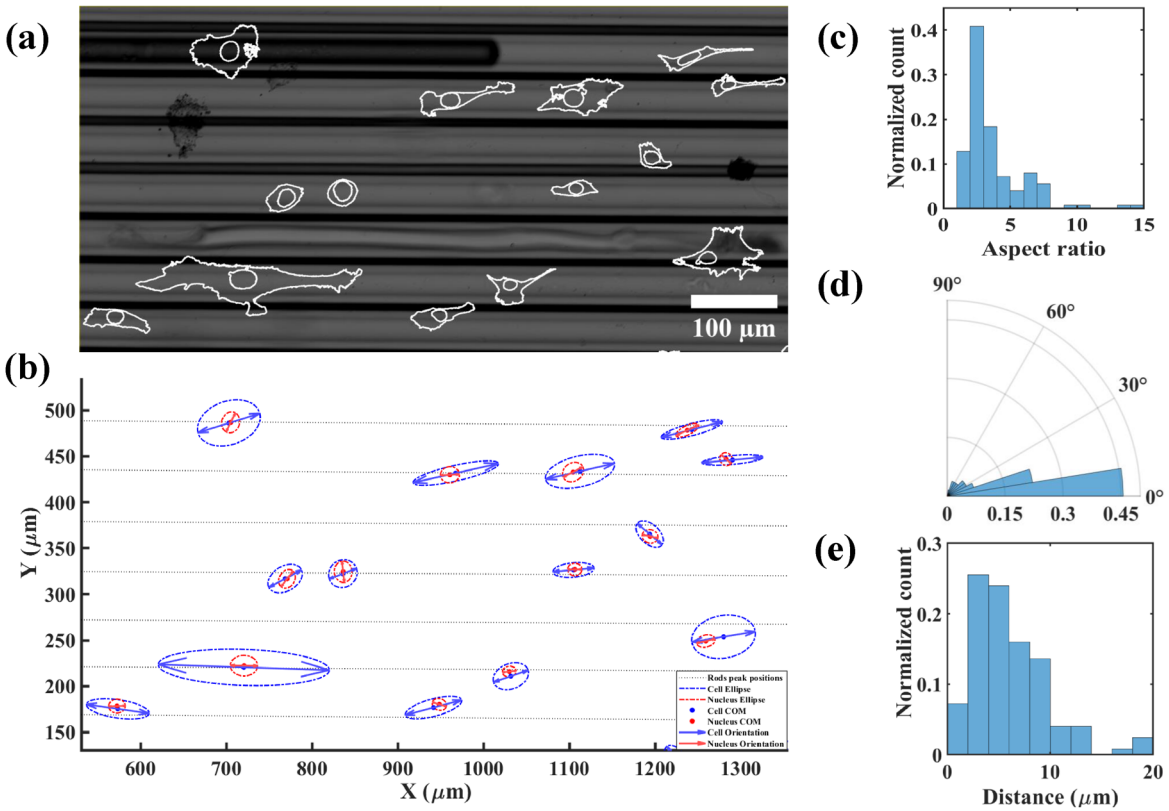

Fig. 4 Shape, orientation, and spatial relationship of cells and nuclei: (a) an example of the image of cells and nuclei with ROIs overlaid to mark regions selected during analysis. (b) Representation of cells (blue) and their corresponding nuclei (red), each fitted to an ellipse to indicate shape and orientation. Arrows illustrate the orientation of the fitted ellipses for both cells and nuclei. The centers of mass for each cell and nucleus are marked. Dashed lines indicate the peak positions of the rods. (c) Cells' aspect ratio distribution. (d) Angular distribution of the orientation differences between cells and their corresponding nuclei. (e) Distribution of the distances between the nuclei COM (center of mass) and their corresponding cells COM. ($N > 120$ cells over $n = 3$ replicates from S-1).

spatial coordinates of the cell on the substrate, but also by the directional stiffness gradient. When cells were positioned in the region of the hydrogel near the peak position of the rod, their motion was nearly one-dimensional along the rod, which is also in the direction of the nearly zero stiffness gradient. The motion was primarily dominated by the horizontal component (large V_x and small V_y) (Fig. 5a). However, the situation is reversed when the cell is positioned far away from the peak of the rod. When the cells were at the peak of the rods, around 60% of the values of the vertical speed were in the range of 0 to 5 μm h^{-1}, and only approximately 8% of the values were higher than 15 μm h^{-1}. However, when the cells were farther from the peak position of the rods, the peak of the distribution of the vertical speed values shifted towards a value higher than 15 μm h^{-1}. For the farthest position of the cells from the peak of the rods, approximately 24% of the vertical speed values were more than 15 μm h^{-1}. In contrast, the distribution of horizontal speed values in different locations showed no significant variation with the relative positions of the cells. Compared to the peak position of the rods, the percentage of horizontal speed values greater than 15 μm h^{-1} increased from approximately 25% to 28% at the farthest position of the cells (see the SI, Fig. S5). From the plots (Fig. 5b and c), the average vertical speed at different cell locations indicates that when the cells were at the peak of the rods, their average vertical speed was 5.7 ± 0.4 μm h^{-1}. This value gradually increased as the cells moved away, reaching a value of 10.4 ± 0.9 μm h^{-1} at locations more than 12 μm from the peak of the rods. However, the average horizontal speed of the cells changed from 11.1 ± 0.9 μm h^{-1} to 12.5 ± 1.4 μm h^{-1} as their position shifted from the peak of the rods to locations more than 12 μm away. It was observed that when cells were located more than 12 μm from the peak of the pattern, there was no significant change in the average values of their vertical and horizontal speeds.

The migration speed data were further corroborated by the location specific dwell time of the cells. When the cells were situated within a ±4 μm region around the peak of the rods, they spent approximately 8.6 ± 0.5 hours during the 20-hour observation period. This value decreased to 3.8 ± 0.3 hours in the subsequent 4 μm region. However, as the cells shifted away from the peak, a rapid decrease in dwell time was observed. At locations greater than 12 μm from the peak of the rods, the dwell time decreased significantly to around 1.7 ± 0.2 hours (Fig. 5d).

From the experimental observations, it was evident that cells preferentially positioned themselves at the peak of the rods,

 This journal is © The Royal Society of Chemistry 2026

Open Access Article. Published on 17 diciembre 2025. Downloaded on 06/03/2026 20:44:40.
This article is licensed under a Creative Commons Attribution-NonCommercial 3.0 Unported Licence.

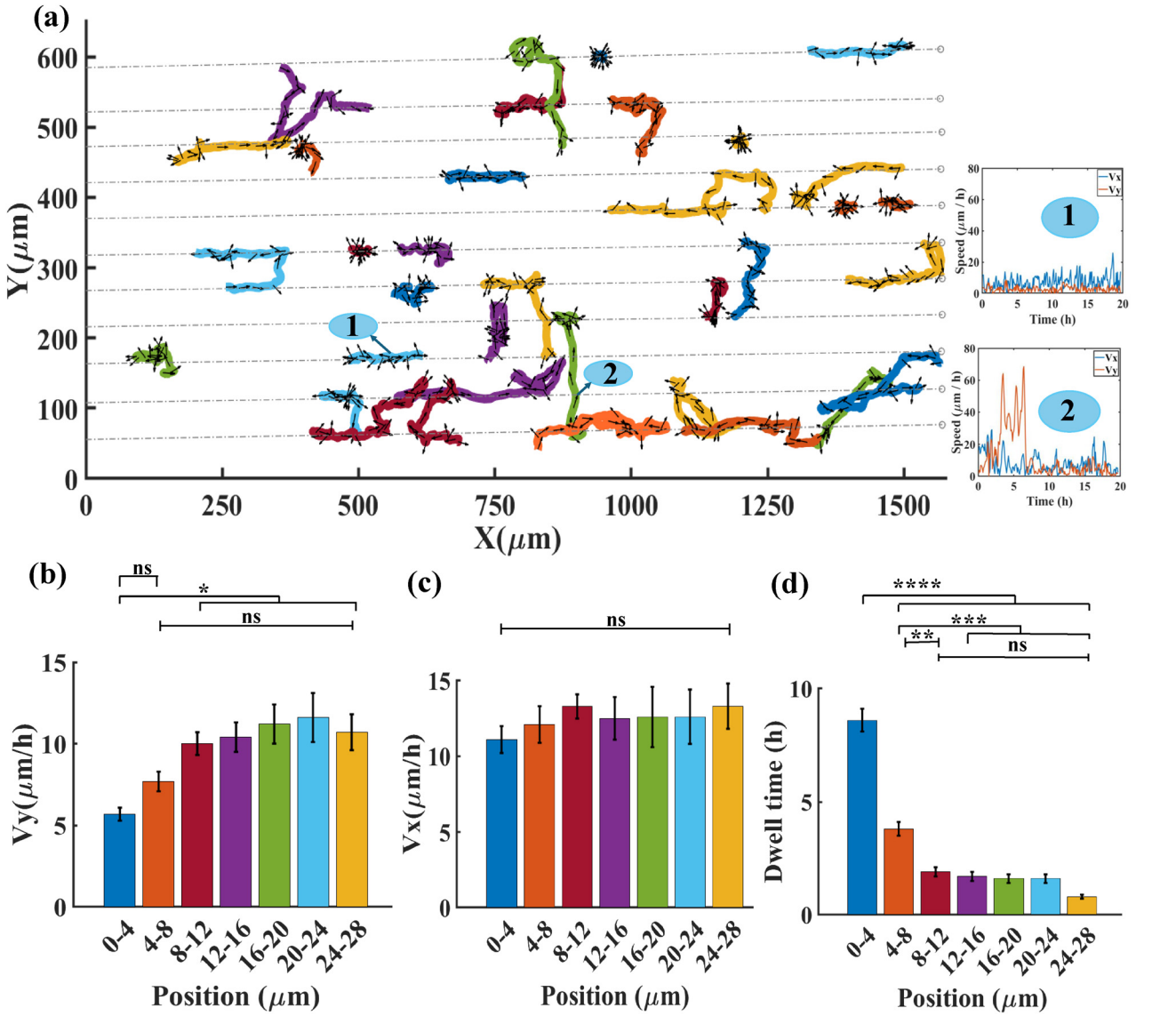

Fig. 5 Location-based cell migration speed and dwell time: (a) trajectories of the ~40 cells over a period of 20 h on substrate S-1. The dashed line represents the peak position of the rods and the inset illustrates the variation in horizontal speed (V_x) and vertical speed (V_y) over time for two cells. One of them moves along the peak position of the rod corresponding to the direction of the minimum rigidity gradient, and the other goes from one rod peak to another rod peak. Cells' movement directions over one-hour intervals are indicated by arrows within each cell's trajectories. (b) and (c) The average vertical and horizontal speed of the cells in different positions, relative to the peak of the rods, respectively ($N > 80$ cells over $n = 4$ replicates of S-1). There is a significant variation in the vertical speed depending on the cells' relative position, while the horizontal speed remains independent of the positioning of the cells on the substrate. (d) Variation in the cells' dwell time based on the duration spent at different relative positions from the peak of the rods of the substrate ($N > 80$ cells over $n = 4$ replicates of S-1). Cells are preferentially positioning themselves near the peak of the rod region. The statistical significance was assessed by one-way ANOVA followed by Tukey's HSD *Post hoc* test (pairwise comparisons) and for all: $^*P < 0.05$, $^{**}P < 0.002$, $^{***}P < 0.0002$, $^{****}p < 0.000001$; ns $p > 0.05$, not significant. Bin size is 4 μm. Error bars are represented here as SE.

where they encountered the minimum stiffness gradient and the highest stiffness. This preference suggests that the mechanical properties at the peak provide an optimal environment for cell adhesion and stability. Additionally, when cells moved away from this peak position, they tended to make a "jump" to return to the same peak or to another peak position within the rods. This behavior was associated with a significant increase in their vertical speed, indicating a dynamic response to the mechanical landscape. Furthermore, the analysis of dwell time supported this observation; cells spent significantly more time at the peaks than at locations further away from the peak. The rapid decrease in dwell time as cells moved away from the peak reinforced the idea that the mechanical properties at the peaks were critical for maintaining cellular stability.

4 Conclusion

Cell adhesion friendly substrates with a very high stiffness gradient are extremely useful in the investigation of durotaxis.

Open Access Article. Published on 17 dicembre 2025. Downloaded on 06/03/2026 20:44:40. This article is licensed under a Creative Commons Attribution-NonCommercial 3.0 Unported Licence.

However, existing methods have been inadequate either in terms of the gradient values they produce or in terms of tunability and robustness. We present a straightforward and reliable approach for fabricating cell-adhesive hydrogel substrates with tunable, cell-scale stiffness gradients by utilizing the topography of an underlying substrate as a template. Fibroblast cells exhibit clear mechanical anisotropy in their response, aligning along the direction of the minimal rigidity gradient and positioning their nuclei toward stiffer regions. The observed threshold in mechanosensitivity suggests saturation of cellular rigidity sensing, which may potentially indicate limits in focal adhesion maturation or cytoskeletal tension. This platform provides a valuable model for dissecting the physical principles underlying mechanotransduction and durotaxis. Overall, this study introduces a versatile platform for investigating cellular responses to mechanical cues across a broad dynamic range. Moreover, this technique offers valuable insights for tissue engineering, wound healing, and regenerative medicine, where the mechanical properties of the extracellular matrix play a decisive role in guiding cell behavior and function.

Author contributions

Indrajit Bhattacharjee: writing – preparing the initial draft, writing, review and editing of the original draft, substrate design conceptualization, methodology, all experimental investigations, data analysis, software validation, and conceptualization. Gautam V. Soni: writing – review and editing of the original draft, proposed the analysis for AFM, and validation. Bibhu Ranjan Sarangi: writing – review, editing, and writing the original draft, project design, project administration, proposed the analysis, validation, funding acquisition, and conceptualization.

Conflicts of interest

There are no conflicts to declare.

Data availability

The data that support the findings of this study are openly available at the following link: https://drive.google.com/drive/folders/178IORLbpJalTnadKETjQNWtOL2nYiDxK?_usp_=_sharingDrive link.

The data supporting this article have been included as part of the supplementary information (SI). Supplementary information is available. See DOI: https://doi.org/10.1039/d5sm00592b.

Acknowledgements

Confocal microscopy was performed at the central instrumentation facility of the Indian Institute of Technology, Palakkad. For AFM experiments, we acknowledge the support of the Raman Research Institute's AFM facility, as well as assistance from Mr Arkabrata Mishra and Mr Yatheendran. The project was supported by funding from the Indian Institute of Technology (ERG Grant-2023-161-PHY-BRS-ERG-SP).

References

1 C.-M. Lo, H.-B. Wang, M. Dembo and Y.-L. Wang, *Biophys. J.*, 2000, **79**, 144–152.
2 A. J. Engler, S. Sen, H. L. Sweeney and D. E. Discher, *Cell*, 2006, **126**, 677–689.
3 R. McBeath, D. M. Pirone, C. M. Nelson, K. Bhadriraju and C. S. Chen, *Dev. Cell*, 2004, **6**, 483–495.
4 T. A. Ulrich, E. M. de Juan Pardo and S. Kumar, *Cancer Res.*, 2009, **69**, 4167–4174.
5 D. E. Jaalouk and J. Lammerding, *Nat. Rev. Mol. Cell Biol.*, 2009, **10**, 63–73.
6 M. J. Paszek, N. Zahir, K. R. Johnson, J. N. Lakins, G. I. Rozenberg, A. Gefen, C. A. Reinhart-King, S. S. Margulies, M. Dembo and D. Boettiger, *et al.*, *Cancer Cell*, 2005, **8**, 241–254.
7 D. E. Discher, P. Janmey and Y.-L. Wang, *Science*, 2005, **310**, 1139–1143.
8 M. A. Wozniak and C. S. Chen, *Nat. Rev. Mol. Cell Biol.*, 2009, **10**, 34–43.
9 B. J. Dickson, *Science*, 2002, **298**, 1959–1964.
10 M. Gupta, B. R. Sarangi, J. Deschamps, Y. Nematbakhsh, A. Callan-Jones, F. Margadant, R.-M. Mège, C. T. Lim, R. Voituriez and B. Ladoux, *Nat. Commun.*, 2015, **6**, 7525.
11 R. Sunyer, A. J. Jin, R. Nossal and D. L. Sackett, *PLoS One*, 2012, **7**, 1–9.
12 I. Bhattacharjee, S. Sudhiram, M. Nithya, B. Kumar and B. R. Sarangi, *Eur. Phys. J.:Spec. Top.*, 2024, 1–9.
13 P. Roca-Cusachs, R. Sunyer and X. Trepat, *Curr. Opin. Cell Biol.*, 2013, **25**, 543–549.
14 B. C. Isenberg, P. A. DiMilla, M. Walker, S. Kim and J. Y. Wong, *Biophys. J.*, 2009, **97**, 1313–1322.
15 B. J. DuChez, A. D. Doyle, E. K. Dimitriadis and K. M. Yamada, *Biophys. J.*, 2019, **116**, 670–683.
16 T. Kawano and S. Kidoaki, *Biomaterials*, 2011, **32**, 2725–2733.
17 S. V. Plotnikov and C. M. Waterman, *Curr. Opin. Cell Biol.*, 2013, **25**, 619–626.
18 Y. S. Choi, L. G. Vincent, A. R. Lee, K. C. Kretchmer, S. Chirasatitsin, M. K. Dobke and A. J. Engler, *Biomaterials*, 2012, **33**, 6943–6951.
19 B. Cortese, G. Gigli and M. Riehle, *Adv. Funct. Mater.*, 2009, **19**, 2961–2968.
20 J. T. Pham, L. Xue, A. Del Campo and M. Salierno, *Acta Biomater.*, 2016, **38**, 106–115.
21 P. Tseng and D. Di Carlo, *Adv. Mater.*, 2013, **26**, 1242.
22 A. Khadpekar, N. Dwivedi, P. Tandaiya and A. Majumder, *Cell Rep. Phys. Sci.*, 2025, **6**, 102456.
23 R. J. Pelham Jr and Y.-L. Wang, *Proc. Natl. Acad. Sci. U. S. A.*, 1997, **94**, 13661–13665.
24 J. A. Burdick, A. Khademhosseini and R. Langer, *Langmuir*, 2004, **20**, 5153–5156.

 This journal is © The Royal Society of Chemistry 2026

Open Access Article. Published on 17 dicembre 2025. Downloaded on 06/03/2026 20:44:40.
This article is licensed under a Creative Commons Attribution-NonCommercial 3.0 Unported Licence.

25 D. Lee, K. Golden, M. M. Rahman, A. Moran, B. Gonzalez and S. Ryu, *Exp. Mech.*, 2019, **59**, 1249–1259.
26 Y. Yang, K. Xie and H. Jiang, *Biophys. J.*, 2020, **119**, 1427–1438.
27 H. Ebata, K. Moriyama, T. Kuboki and S. Kidoaki, *Biomaterials*, 2020, **230**, 119647.
28 S. Kidoaki and T. Matsuda, *J. Biotechnol.*, 2008, **133**, 225–230.
29 D. Joaquin, M. Grigola, G. Kwon, C. Blasius, Y. Han, D. Perlitz, J. Jiang, Y. Ziegler, A. Nardulli and K. J. Hsia, *Biotechnol. Bioeng.*, 2016, **113**, 2496–2506.
30 C.-H. R. Kuo, J. Xian, J. D. Brenton, K. Franze and E. Sivaniah, *Adv. Mater.*, 2012, **24**, 6059–6064.
31 H. Zhang, F. Lin, J. Huang and C. Xiong, *Acta Biomater.*, 2020, **106**, 181–192.
32 H. Zhang, Y. Ma, W. Shu, Y. Wang, C. Cao, W. Wan, N. Shi, Z. Wei, D. Pei and A. Li, *et al.*, *Adv. Funct. Mater.*, 2024, **34**, 2309676.
33 Y. Shu, H. N. Chan, D. Guan, H. Wu and L. Ma, *Sci. Bull.*, 2017, **62**, 222–228.
34 A. Buxboim, K. Rajagopal, B. Andre'EX and D. E. Discher, *J. Phys.: Condens. Matter*, 2010, **22**, 194116.
35 J. M. Maloney, E. B. Walton, C. M. Bruce and K. J. Van Vliet, *Phys. Rev. E:Stat., Nonlinear, Soft Matter Phys.*, 2008, **78**, 041923.
36 S. Sen, A. J. Engler and D. E. Discher, *Cell. Mol. Bioeng.*, 2009, **2**, 39–48.
37 J. R. Tse and A. J. Engler, *Curr. Protoc. Cell Biol.*, 2010, **47**, 10–16.
38 S. Syed, J. Schober, A. Blanco and S. Zustiak, *PLoS One*, 2017, **12**(11), e0187853.
39 H.-J. Butt and M. Jaschke, *Nanotechnology*, 1995, **6**, 1.
40 M. D. Norman, S. A. Ferreira, G. M. Jowett, L. Bozec and E. Gentleman, *Nat. Protoc.*, 2021, **16**, 2418–2449.
41 Y.-R. Chang, V. K. Raghunathan, S. P. Garland, J. T. Morgan, P. Russell and C. J. Murphy, *J. Mech. Behav. Biomed. Mater.*, 2014, **37**, 209–218.
42 A. M. Smith, D. G. Inocencio, B. M. Pardi, A. Gopinath and R. C. Andresen Eguiluz, *ACS Appl. Poly. Mater.*, 2024, **6**, 2405–2416.
43 C. E. Kandow, P. C. Georges, P. A. Janmey and K. A. Beningo, *Methods Cell Biol.*, 2007, **83**, 29–46.
44 F. J. Byfield, Q. Wen, I. Levental, K. Nordstrom, P. E. Arratia, R. T. Miller and P. A. Janmey, *Biophys. J.*, 2009, **96**, 5095–5102.
45 U. Schmidt, M. Weigert, C. Broaddus and G. Myers, Medical Image Computing and Computer-Assisted Intervention-MICCAI 2018: 21st International Conference, Granada, Spain, September 16-20, 2018, Proceedings, Part III 21, 2018, pp. 265–272.
46 D. Ershov, M.-S. Phan, J. W. Pylvänäinen, S. U. Rigaud, L. Le Blanc, A. Charles-Orszag, J. R. Conway, R. F. Laine, N. H. Roy and D. Bonazzi, *et al.*, *Nat. Methods*, 2022, **19**, 829–832.
47 K. Moriyama and S. Kidoaki, *Langmuir*, 2018, **35**, 7478–7486.
48 A. Ueki and S. Kidoaki, *Biomaterials*, 2015, **41**, 45–52.
49 J. Solon, I. Levental, K. Sengupta, P. C. Georges and P. A. Janmey, *Biophys. J.*, 2007, **93**, 4453–4461.
50 F. J. Calero-Cuenca, C. S. Janota and E. R. Gomes, *Curr. Opin. Cell Biol.*, 2018, **50**, 35–41.